Arbitrary crack propagation in multi-phase materials using the finite volume method

D. Carolan[a,*], Ž. Tuković[b], N. Murphy[a], A. Ivanković[a]

[a] *School of Mechanical and Materials Engineering, University College Dublin, Ireland*
[b] *Faculty of Mechanical Engineering and Naval Architecture, University of Zagreb*

Abstract

An arbitrary crack propagation model using cell-centre finite volume based method is presented. Crack growth in an elastic solid, across an interface perpendicular to the initial crack path and into a second elastic solid is analysed. Crack initiation and the subsequent path of propagation are shown to arise naturally out of the selection of appropriate cohesive parameters. It is shown that the allowable crack propagation path is restricted by the underlying mesh. Results are presented for a number of values of interfacial strength and ratios of elastic properties between the two elastic solids. For higher values of interfacial strength, the crack is shown to propagate straight through the interface, while for lower values of interfacial strength, the crack is shown to change direction and propagate along the interface. It is shown that with careful selection of material and interface parameters it is possible to arrest a propagating crack at the interface. The method represents a useful step towards the prediction of crack propagation in complex structures.

Keywords: brittle fracture, cohesive zone model, finite volume method,

*Corresponding Author
Email address: declan.carolan@ucd.ie (D. Carolan)

1. Introduction

The mechanical and fracture properties of many engineering materials are affected by the underlying microstructure of the material. For this reason it is important to be able to correctly predict the stresses, crack initiation and propagation of a complex microstructure. In this paper a finite-volume based method for the solution of fracture problems containing multiple dissimilar materials in which the crack path is not prescribed a priori is presented. In the current work the direction of crack propagation is limited only by the position and orientation of internal faces in the chosen numerical mesh.

Over the last number of years the Finite Volume (FV) method has become established as an alternative to the Finite Element Method for the solution of problems involving stress analysis. The method was first developed for the solution of solid mechanics problems by Demirdžić and co-workers [1–5]. Ivanković and co-workers have applied the FV method successfully to the solution of both fracture problems [6–9] and fluid structure interaction problems [10, 11].

Recently, Tuković et al. [12] have developed a finite-volume based method to accurately calculate tractions at the interface of two or more dissimilar solid materials. Due to the difference in elastic properties of the constituent material they showed that the interface can be a potential source of the onset of damage.

Much work has been carried out to study the interaction between a stationary crack close to an interface [13, 14]. In particular, He and Hutchinson

[15] considered the competition between deflection and penetration of a crack at the interface for a crack approaching the interface at different angles. He and Hutchinson [16] analysed the conditions under which an interface crack will kink out of an interface. He et al. [17] have also examined the role of residual stress in determining the crack path.

He and Hutchinson [15] have shown that the solution of simple plane strain, traction boundary value problems, the solution depends only on the non-dimensional Dundurs' parameters, α and β [18]. For plane stress conditions, the parameters are given as:

$$\alpha = \frac{k(\kappa_1 + 1) - (\kappa_2 + 1)}{k(\kappa_1 + 1) + (\kappa_2 + 1)} \tag{1}$$

$$\beta = \frac{k(\kappa_1 - 1) - (\kappa_2 - 1)}{k(\kappa_1 + 1) + (\kappa_2 + 1)} \tag{2}$$

where k is the ratio of shear moduli, μ_2/μ_1 and κ_i is Muskhelishwili's constant [19], equal to $(3 - 4\nu_i)$, where ν_i is the Poisson's ratio of material i.

Further, they present a ratio in terms of α and β, which allows one to assess the relative tendency of a crack to be deflected into an interface or to penetrate through it. The ratio is given as:

$$\frac{G_d}{G_p} = \left(\frac{1 - \beta^2}{1 - \alpha}\right) \frac{|d|^2 + |e|^2 + 2\mathrm{Re}(de)}{c^2} \tag{3}$$

where G_d/G_p is the ratio of the energy required for crack $d$eflection along the interface versus crack $p$enetration through the interface, α and β are the Dundur's parameters and c, d and e are complex valued functions of α and β. The ratio, G_d/G_p as a function of α is plotted in Figure 1 for $\beta = 0$.

For α not too different to zero, the critical ratio is approximately 0.25. This corresponds to a case where the elastic properties are the same either

side of an interface. The critical ratio increases to approximately 0.38 when $\alpha = 0.33$, corresponding to a modulus factor difference of two across a material interface. If the ratio of interface cohesive strength, σ_{max}^{int} to bulk cohesive strength, σ_{max}^{bulk} is less than the critical ratio then the crack will deflect into the interface and propagate along the interface rather than penetrate the interface directly.

Siegmund et al. [20] used the finite element method to numerically predict the crack path of a crack propagating in an an elastic solid, across and interface and into an elastic visco-plastic solid. They successfully recovered the predictions of [15]. For an interface with a cohesive strength less than 25% of the bulk material strength the crack is deflected into the interface rather than propagating through into the second material. They also show that with appropriate selection of plastic parameters in the second material the propagating crack can be permanently arrested at the interface.

This paper describes the application of the finite volume method to the solution of complex crack propagation problems in a multi-material linear-elastic model. All numerical procedures described are implemented in OpenFOAM [21, 22].

2. Numerical Model

An isothermal multi-material linear elastic model is considered where the behaviour is described by conservation of momentum law and linear elastic constitutive relation:

$$\int_V \rho \frac{\partial^2 \mathbf{u}}{\partial t^2} \mathrm{d}V = \oint_S \mathbf{n} \cdot \boldsymbol{\sigma} \mathrm{d}S \tag{4}$$

$$\boldsymbol{\sigma} = \mu[\nabla \mathbf{u} + (\nabla \mathbf{u})^T] + \lambda \mathrm{tr}(\nabla \mathbf{u})\mathbf{I} \tag{5}$$

where ρ is the density of the material with volume V, $\mathbf{n}$ is the normal to the surface S, $\mathbf{u}$ is the displacement vector with respect to initial configuration, $\boldsymbol{\sigma}$ is the Cauchy stress tensor and μ and λ are the Lamé coefficients.

As shown in [12], the normal and tangential components of the traction vector $\mathbf{t} = \mathbf{n} \cdot \boldsymbol{\sigma}$ can be expressed in terms of displacement vector $\mathbf{u}$ using constitutive equation (5) as follows:

$$\mathbf{t}_n = (2\mu + \lambda)\mathbf{n} \cdot \nabla\mathbf{u} - (\mu + \lambda)\mathbf{n} \cdot \nabla\mathbf{u}_t + \lambda\mathbf{n}\mathrm{tr}(\nabla_t\mathbf{u}_t) \tag{6}$$

$$\mathbf{t}_t = \mu\mathbf{n}.\nabla\mathbf{u}_t + \mu\nabla_t u_n \tag{7}$$

where $\nabla_t = (\mathbf{I} - \mathbf{nn}) \cdot \nabla$ is the tangential gradient operator and the subscripts n and t represent the normal and tangential components of the vector. Equations (6) and (7) are valid up to the interface but not across the interface due to discontinuity of displacement gradient across the interface. The derivation of the correction traction at the interface can be found in Tuković et al. [12].

The mathematical model described above is discretised in space using second order accurate collocated unstructured FV method while numerical integration of the model in time is performed using first (or second) order accurate implicit method.

According to unstructured FV discretisation, computational space is in general divided into a finite number of convex polyhedral control volumes (CV) or cells bounded by convex polygons (faces). The cells do not overlap and fill the spatial domain completely. Figure 2 shows a simple polyhedral control volume V_P around the computational point P located in its centroid, the face f, the face area S_f, the face unit normal vector $\mathbf{n}_f$ and the centroid N of the neighbouring CV sharing the face f.

In this study it is assumed that an interface between different elastic materials coincides with the internal CV faces. In general, however, a CV can be bounded by a combination of ordinary internal faces, internal faces at the multi-material interface and boundary faces.

Details of FV discretization of the considered mathematical model can be found in [12], where special attention is paid to discretization of traction force at the multi-material interface.

The arbitrary crack propagation model implemented allows prediction of crack propagation along internal control volume faces [23]. An internal control volume face at which the failure criterion is satisfied is turned into a pair of cohesive zone boundary faces. The traction force specified between these cohesive zone faces is governed by the cohesive zone model. The cohesive zone model works on the basis that all the damage processes taking place locally ahead of the crack tip can be described by a unique stress-displacement relationship as shown in Figure 3. For the simplest models, two parameters are required to fully describe the model. These are the fracture energy G_c and the maximum cohesive strength σ_{max}. According to the cohesive zone model the traction between cohesive zone faces is a function of the separation distance between the faces. In case of mode I (opening) crack, only normal separation distance is considered and the traction-separation law defines normal cohesive traction between cohesive faces as a function of normal separation distance. Once the critical traction, σ_{max} is the normal cohesive traction, σ decreases from the critical traction to zero traction according to the specified traction-separation curve. When the critical normal separation δ_c is reached, fracture is assumed to have taken place and the cohesive faces

are thereafter treated as traction-free faces.

In the case of opening mode I crack, failure of a face occurs when $t_n \geq \sigma_{max}$. The normal cohesive traction between the faces is then defined by the cohesive zone model. If there is a shear component of traction on the face, the cohesive shear traction behaviour is assumed to have the same shape as the normal cohesive traction behaviour as assumed by Camacho and Ortiz [24].

In the case of mixed mode I and II crack, the failure criteria for internal face is defined as:

$$t_{eff} = \sqrt{t_n^2 + |\mathbf{t}_t|^2} \geq \sigma_{max} \tag{8}$$

where t_n and $\mathbf{t}_t$ are normal and tangential components of traction on any internal face described earlier. The traction between the cohesive faces is then expressed as a function of effective separation distance, δ_{eff}:

$$\delta_{eff} = \sqrt{\delta_n^2 + \delta_t^2} \tag{9}$$

where δ_n is the normal separation distance and δ_t is the tangential separation distance. For a linear traction separation law the normal and tangential cohesive tractions, $\mathbf{t}_{cn}$ and $\mathbf{t}_{ct}$, are then given as:

$$\mathbf{t}_{cn} = \mathbf{t}_{0n}\left(1 - \frac{\delta_{eff}}{\delta_c}\right) \tag{10}$$

$$\mathbf{t}_{ct} = \mathbf{t}_{0t}\left(1 - \frac{\delta_{eff}}{\delta_c}\right) \tag{11}$$

where $\mathbf{t}_{0n}$ and $\mathbf{t}_{0t}$ are the initiation tractions in the normal and tangential directions respectively and δ_c is the critical opening displacement.

The solution procedure is given in Figure 4. At the end of each time step calculation, the traction at each internal cell is determined and all faces

for which the failure criterion is satisfied are gathered together and ordered according to traction. The face with the highest traction level is broken. The internal face is transformed into two cohesive boundary faces. The time step calculation is then repeated. This procedure is repeated until there are no more broken faces.

In all of the simulations examined in this work, a linear traction separation law was specified. The cohesive strength, σ_{max} of the bulk material was kept constant at 200 MPa and the fracture energy, G_c was 100 J/m^2. The ratio of Mode I cohesive parameters to Mode II cohesive parameters was set to one in all cases.

3. Results

To validate the developed procedure a simple problem is considered. A simple bi-material specimen with a centrally located crack oriented perpendicular to the bi-material interface as shown in Figure 5 is analysed. The initial crack length, a is 0.3 mm, while the half-width L and half-length W are 1.5 mm and 3 mm respectively. The interface is located at $L/2$.

A time varying fixed displacement is applied to the top and bottom boundaries corresponding to a displacement rate, v, of 0.0167 m/s. The left hand boundary is modeled as a symmetry plane while the right hand boundary is modeled as traction free. The model is 2-dimensional and plane stress is assumed. The mesh was created using `blockMesh`, a utility within OpenFOAM for creating structured hexahedral meshes, and is a fully orthogonal hexahedral grid containing 300×300 cells in x and y directions and 1 in the z direction that is not solved. The mesh density was chosen arbitrarily

to allow the simulations to solve in a reasonable amount of time.

In all cases a linear cohesive zone formulation is assumed. For simplicity the cohesive zone parameters uniform throughout both materials. The cohesive properties of the interface differ from those in the bulk material, i.e. $\sigma_{max}^{int} = m\sigma_{max}^{bulk}$, where m is some fraction between 0 and 1. The allowable cohesive zone formulations at the interface are restricted such that the critical opening displacement ($\propto G_c/\sigma_{max}$) is unchanged from the bulk material where E is the plane stress Young's modulus of the bulk material, and G_c is the strain energy release rate. Thus, if $\sigma_{max,i} = m\sigma_{max}^{bulk}$, then $G_c^{int} = mG_c^{bulk}$.

The limiting crack speed in a linear elastic material is known to be proportional to the speed of sound for one dimensional wave propagation, $c_0 = \sqrt{E/\rho}$. Roberts and Wells [25] have shown analytically that the crack limiting speed, $\dot{a}$, is equal to $0.38c_0$, while Freund [26] has calculated numerically for $\nu = 0.3$, $\dot{a} = 0.57c_0$. Therefore, it is appropriate to choose c_0 as an extremely conservative upper limiting speed. An upper limit on the time step interval for the crack propagation phase of the simulation can then be calculated based on this upper crack limiting speed.

The time,t, taken for a crack propagating at a velocity, c_0 along a control volume face of length l_f is given by $t = l_f/c_0$. For the problems investigated, the maximum value of c_0 is 5.18 km/s (E = 210 GPa, ρ = 7800 kg/m^3) and thus t = 1.95 ns for the mesh of size 300×300 respectively. This value represents a limiting time step during the crack propagation phase of the simulation to ensure that only one internal face is cracked per time step and that all the crack propagation behaviour is captured during the simulation. In order to further ensure that the time step was sufficiently small, the minimum

time step in the simulation was set to 1 ns during crack propagation. In order to speed up the initial loading/initiation portion of the simulation a much larger time step of 0.1 μs was employed. This time step was gradually reduced to the limiting time step once the traction directly ahead of the crack tip reached 90% of the initiation value.

The effect of varying the cohesive properties of the interface on crack initiation, propagation, and path is investigated for four cases: (1) $E_1 = E_2 =$ 210 GPa, (2) $E_1 = 210$ GPa, $E_2 = 420$ GPa, (3) $E_1 = 210$ GPa, $E_2 = 630$ GPa and (4) $E_1 = 210$ GPa, $E_2 = 105$ GPa. Poisson's ratio, $\nu = 0.3$ is kept constant in all cases. Once the crack reaches a boundary face, the simulation is stopped. In case (1) the effect of mesh density on the final crack path is investigated.

3.1. Case 1: $E_1 = E_2 = 210$ GPa

Figure 6 shows the final crack path for the case where the elastic properties of both materials are equal and where the σ_{max}^{int} is, (a) 0.1, (b) 0.2 and (c) 0.3 times the cohesive strength of the bulk material respectively. It can be clearly seen that there is crack propagation along the interface for the cases where the ratio, $\sigma_{max}^{int}/\sigma_{max}^{bulk}$ is less than the critical ratio of 0.25.

In the case of (a), the crack propagates for a distance of 0.3 mm up and down the interface before changing direction and propagating into material 2. There is continued crack propagation along the interface at this point but at a greatly reduced rate than in the second material.

If the value of σ_{max}^{int} is raised to 0.2 times the bulk cohesive strength as in (b) the crack also propagates to the interface and begins to propagate along the interface. However, there is only 0.1 mm of propagation along the

interface before the original crack penetrates the interface and propagates directly through material 2. As before there is concurrent crack extension along the interface after penetration of the main crack in to material 2 but at a reduced rate.

The crack path in (c) is simpler to analyse. The ratio of interface cohesive strength to bulk cohesive strength is significantly higher than the critical ratio required to deflect the crack into the interface. Therefore, the crack penetrates directly into material 2 and the relative strength at the interface does not play any role in determining the crack path.

3.1.1. Effect of mesh density

Figure 7 plots the effect of reduced mesh density on the predicted crack propagation paths. A mesh of (a) 75×75 cells and (b) 150×150 cells were employed, reducing the area of a face by one quarter and one half respectively over the original mesh. It can be seen that there is an asymmetry in the crack patterns in material 2 in both Figure 7 (a) and Figure 7 (b).

This highlights the fact that numerical asymmetry can occur in this problem if insufficient care is taken to produce an adequate mesh prior to simulation. As explained previously, each internal face exceeding the critical traction in a particular time step is ordered and fractured sequentially according to the absolute value of traction across the face. The face immediately next to the upper crack in Figure 7 (a) had a slightly higher traction across the face than in the lower crack and consequently separated before the corresponding face in the lower crack. On updating the boundary conditions, the traction in the next face in the upper crack then exceeded the traction in the face immediately ahead of the lower crack and so it was fractured at the

expense of the lower crack. It can be seen that a finer mesh, Figure 7 (b), reduces this problem.

3.1.2. Crack growth in a trigonal cell based mesh

The problem presented so far was modeled using a perfectly orthogonal hexahedral mesh. This is due to the simplicity of the geometry being investigated. Many problems encountered in reality will have much more complex geometries than that previously described. In order to demonstrate the applicability of the arbitrary crack propagation simulation on a different mesh, Case 1 is simulated using a trigonal cell based mesh.

To this end, a mesh containing 8,186 cells was created using third party meshing software. Figure 8 shows the final crack path and the mesh detail close to the material interface. It can be seen that there is reasonably good agreement in the crack path prediction between the perfectly orthogonal hexagonal mesh originally investigated, Figure 6 (a) and the mesh presented in Figure 8. Both simulations present the same gross features, crack propagation in material 1 to the interface followed by propagation along the interface and finally penetration into material 2 at two locations along the interface.

However, the variation in crack path between the two cases demonstrates the fact that the allowable crack propagation path is predetermined by the mesh. Therefore care is still needed when meshing complex geometries to ensure that the direction of crack propagation should be as independent of the underlying mesh as possible. A systematic mesh refinement would be required for complex geometries where the possible crack paths are completely unknown in order to determine a unique mesh independent solution.

3.2. Case 2: $E_1 = 210\ GPa,\ E_2 = 420\ GPa$

In this case the Dundur's parameters are non-zero and one can calculate, $\alpha = 1/3$, and $\beta = 2/15$. The corresponding critical ratio for cohesive strengths is approximately 0.4. Therefore, one would expect to observe some level of crack deflection into the interface below 0.4 with penetration of the crack through the interface observed for any ratio of cohesive strength greater than 0.4. An inspection of Figure 9 reveals that this is indeed the case. When $\sigma_{max}^{int}/\sigma_{max}^{bulk} = 0.5$, no crack deflection at the interface is noted whereas for $\sigma_{max}^{int}/\sigma_{max}^{bulk} = 0.1$ and 0.3 varying degrees of crack growth along the interface is noted.

3.3. Case 3: $E_1 = 210\ GPa,\ E_2 = 630\ GPa.$

According to He and Hutchinson [15] the critical ratio for crack deflection at the interface for $E_3/E_1 = 3$ is approximately 0.5. Figure 10 presents the final crack paths for ratios of 0.2, 0.4 and 0.6 respectively. It can be seen that below the critical ratio some crack growth along the interface is noted with the amount of crack growth decreasing as the critical ratio is approached. Above the critical ratio the crack penetrates the interface and no interface crack growth is observed.

In all three cases investigated the total crack growth rate increases, Figure 11, as a result of entering the stiffer material. The onset of bifurcation occurs slightly later in order to absorb the excess energy being delivered to the crack front, at which point the global crack growth rate is observed to increase once again.

3.4. Case 4: $E_1 = 210$ *GPa,* $E_2 = 105$ *GPa.*

The corresponding Dundur's parameters for this case are: $\alpha = -1/3$, $\beta = -2/15$. The critical ratio for crack deflection according to He [15] is approximately 0.2. Figure 12 presents the final crack paths for ratios of $\sigma^{int}_{max}/\sigma^{bulk}_{max}$ of 0.1, 0.2 and 0.3 respectively. The crack growth for each of these case versus time is given in Figure 13.

It can be clearly seen that when the interface cohesive strength is 10% of the bulk cohesive strength the crack deflects into the interface and propagates entirely along the interface. Unlike the case presented in 6 (b) the crack does not penetrate material 2. This is because the energy requirements required to advance the crack into the lower modulus material 2 are not met. The crack length history curve in 13 indicates that the rate of crack growth is barely retarded by deflection to the interface.

A comparison of the crack length history for $\sigma^{int}_{max}/\sigma^{bulk}_{max} = 0.2$ and 0.3 in Figure 13 indicates that the behaviour is not what might be intuitively expected. It appears that the crack in 20% interface strength model retards earlier, at $\Delta a = 1.32$ mm, than for the 30% case, $\Delta a = 1.86$ mm. Furthermore, crack arrests for longer in the 20% case than the 30% case. For the 20% model, the crack propagates to the interface as before and is then deflected into the interface where it propagates a small amount as shown in Figure 12 (b) before arresting. Continued crack growth in material 2 occurs at 0.0285 s and no subsequent propagation is noted at the interface. In the 30% case the initial crack grows, and penetrates the interface without retardation before arresting 0.6 mm into material 2 by virtue of the fact that material 2 is more compliant. Crack growth continues earlier than in the 20% case as the stress

intensity factor is greater for the single crack tip than the branched crack at the interface shown in Figure 12 (b).

The fact that there exists a certain preferential cohesive interface strength between phases which promotes crack arrest in a composite material has important ramifications for the design of structural composite materials. If the interface strength is too low, the crack will quickly propagate along the interface, too high and the crack will penetrate the second phase.

4. Conclusions

A finite-volume based multi-material arbitrary crack propagation procedure developed in OpenFOAM was presented. Particular attention was paid to the correct calculation of tractions at a multi material interface. The procedure was validated against a classic problem in the literature. The results show that the procedure is capable of reproducing the predictions of He and Hutchinson [15] for a crack approaching a bimaterial interface. It has also been shown that the crack propagation path is influenced by the choice of mesh since the crack can only propagate along the cell faces.

The importance of precisely understanding the role of the interface in crack path selection has been demonstrated and it has been shown that for given material combinations there exists a preferential interface strength which maximises the ability of a composite material to successfully retard a propagating crack.

5. Acknowledgements

The authors would like to acknowledge the financial support of *Element 6 Ltd* and *Enterprise Ireland*.

References

[1] I. Demirdžić, D. Martinović, A. Ivanković, Numerical simulation of thermal deformation in welded specimens (in croatian), Zavarivanje 31 (1988) 209–219.

[2] I. Demirdžić, D. Martinović, Finite volume method for thermo-elasto-plastic stress analysis, Computer Methods in Applied Mechanics and Engineering 109 (1993) 331–349.

[3] I. Demirdžić, S. Muzaferija, Finite volume method for stress analysis in complex domains, International Journal for Numerical Methods in Engineering 37 (1994) 3751–3766.

[4] I. Demirdžić, S. Muzaferija, Numerical method for coupled fluid flow, heat transfer and stress analysis using unstructured moving meshes with cells of arbitrary topology, Computer methods in Applied Mechanics and Engineering 125 (1995) 235–255.

[5] I. Demirdžić, E. Džaferović, A. Ivanković., Finite volume approach to thermoviscoelasticity, Numerical Heat Transfer, Part B 47 (3) (2005) 213–237.

[6] A. Ivankovic, I.Demirdzic, J. Williams, P. Leevers, Application of the finite volume method to the analysis of dynamic fracture problems, International Journal of Fracture 66 (1994) 357–371.

[7] A. Ivanković, S. Muzaferija, I.Demirdzic, Finite volume method and multigrid acceleration in modelling of rapid crack propagation in full-scale pipe test, Computational Mechanics 20 (1997) 46–52.

[8] A. Ivankovic, Finite volume modelling of dynamic fracture problems, Computer Modelling and Simulation in Engineering 4 (1999) 227–235.

[9] A. Ivanković, K. Pandya, J. Williams, Crack growth predictions in polyethylene using measured traction-separation curves, Engineering Fracture Mechanics 71 (2004) 657–668.

[10] V. Kanyanta, A. Karac, A. Ivankovic, Validation of a fluid structure interaction numerical model for predicting flow transients in arteries, Journal of Biomechanics 42 (2009) 1705–1712.

[11] A. Karac, A. Ivankovic, Investigating the behaviour of fluid-filled polyethylene containers under base drop impact: A combined experimental/numerical approach, International Journal of Impact Engineering 36 (2009) 621–631.

[12] Ž. Tuković, A. Ivanković, A. Karač, Finite volume stress analysis in multi-material linear elastic body, International Journal for Numerical Methods in Engineering, doi: 10.1002/nme.4390.

[13] T. Cook, F. Erdogan, Stresses in bonded materials with a crack perpendicular to the interface, International Journal of Engineering Science 10 (1972) 677–697.

[14] F. Erdogan, V. Biricikoglu, Two bonded half planes with a crack going going through the interface, International Journal of Engineering Science 11 (1975) 745–766.

[15] M. He, J. Hutchinson, Crack deflection at an interface between dissimilar materials, International Journal of Solids and Structures 25 (1989) 1053–1067.

[16] M. He, J. Hutchinson, Kinking of a crack out of an interface, Journal of Applied Mechanics 111 (1989) 270–278.

[17] M. He, A. Evans, J. Hutchinson, Crack deflection at an interface between dissimilar elastic materials: Role of residual stresses, International Journal of Engineering Science 11 (1975) 745–766.

[18] J. Dundurs, Edge-bonded dissimilar orthogonal elastic wedges, Journal of Applied Mechanics 36 (1969) 650–662.

[19] N. Muskhelishwili, Some Basic Problems of the Mathematical Theory of Elasticity, R. Noordhoff Publ. Company, Groningen, Netherlands, 1953.

[20] T. Siegmund, N. Fleck, A. Needleman, Dynamic crack growth across an interface, International Journal of Fracture 85 (1997) 381–402.

[21] H. Weller, G. Tabor, H. Jasak, C. Fureby, A tensorial approach to CFD

using object oriented techniques, Computers in Physics 12 (1998) 620–631.

[22] OpenFOAM, www.wikki.co.uk, www.openfoam.co.uk (2011).

[23] N. Murphy, A. Ivankovic, The prediction of dynamic fracture evolution in PMMA using a cohesive zone model, Engineering Fracture Mechanics 72 (2005) 861–875.

[24] G. Camacho, M. Ortiz, Computational modelling of impact damage in brittle materials, International Journal of Solids and Structures 33 (1996) 2899–2938.

[25] D.K. Roberts, A.A. Wells, The velocity of brittle fracture, Engineering 178 (1954) 820–821.

[26] L.B. Freund, Crack propagation in an elastic solid subjected to general loading - I. Constant rate of extension, Journal of the Mechanics and Physics of Solids 20 (1972) 141–152.

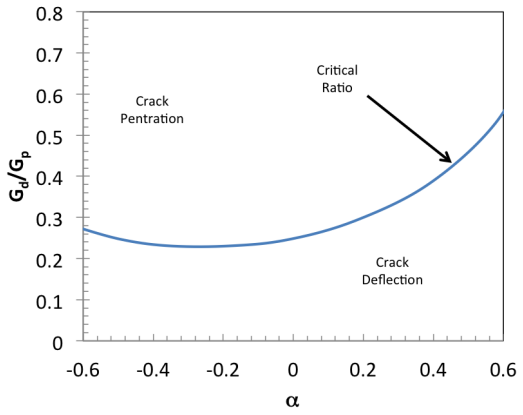

Figure 1: Critical ratio of interface strength versus bulk material strength for crack deflection versus crack penetration as a function of α. Data reproduced from [15]

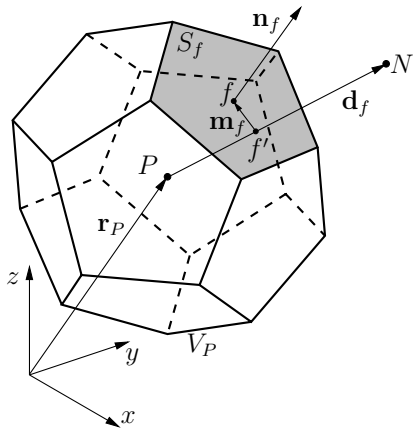

Figure 2: Polyhedral control volume (cell).

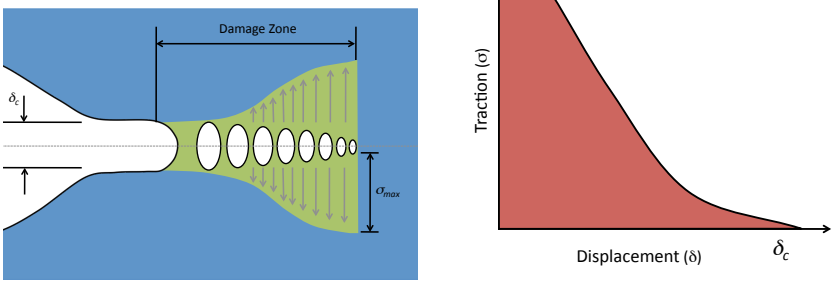

(a) Damage zone ahead of a growing crack.

(b) General form.

Figure 3: A cohesive zone model.

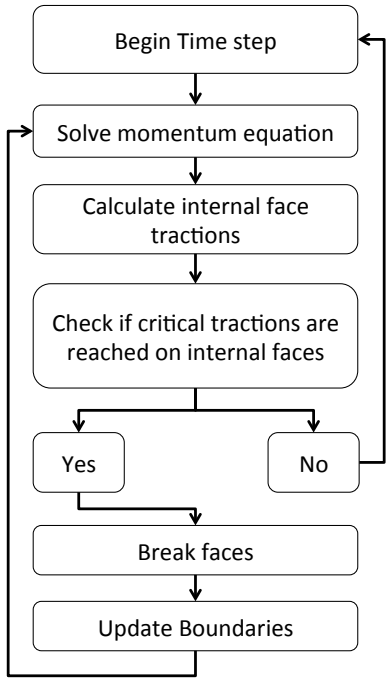

Figure 4: Solution flow diagram for arbitrary crack propagation procedure.

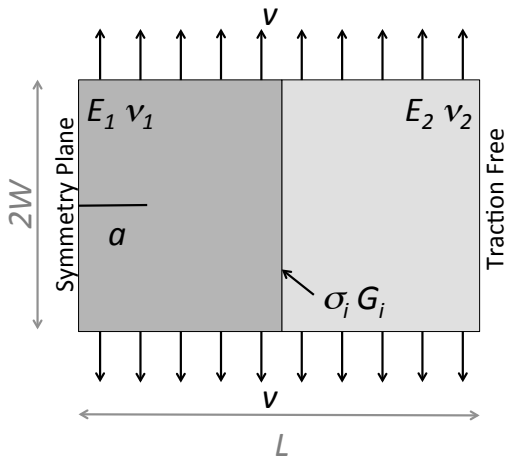

Figure 5: Geometry of the centre crack bi-material specimen.

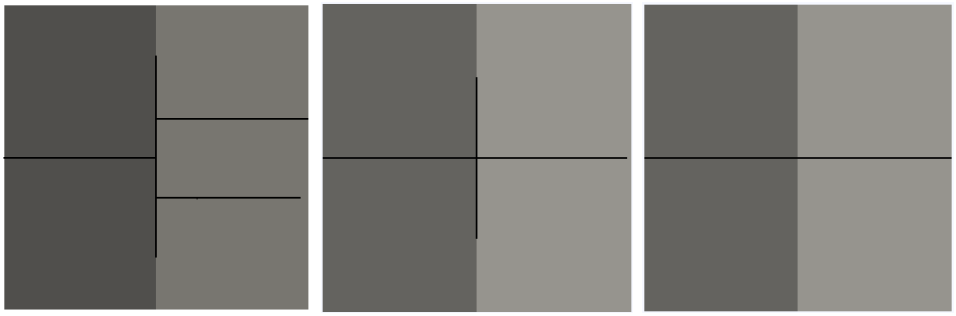

(a) $\sigma_{max}^{int} = 0.1(\sigma_{max}^{bulk})$. (b) $\sigma_{max}^{int} = 0.2(\sigma_{max}^{bulk})$. (c) $\sigma_{max}^{int} = 0.3(\sigma_{max}^{bulk})$.

Figure 6: Final crack paths for $E_1 = E_2 = 210$ GPa.

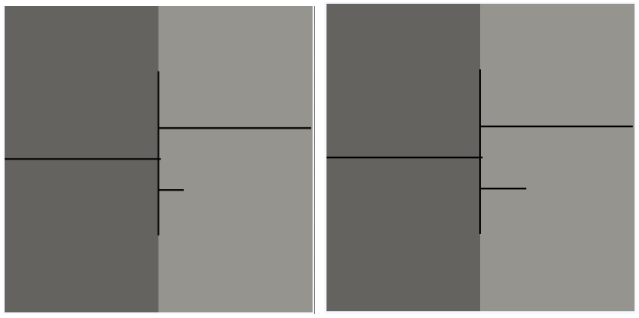

(a) 75 by 75 cells. (b) 150 by 150 cells.

Figure 7: Effect of mesh density on the final crack paths for Case 1.

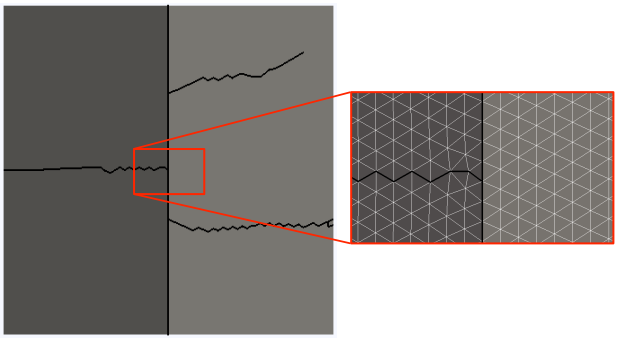

Figure 8: Crack path predictions using a trigonal cell based mesh.

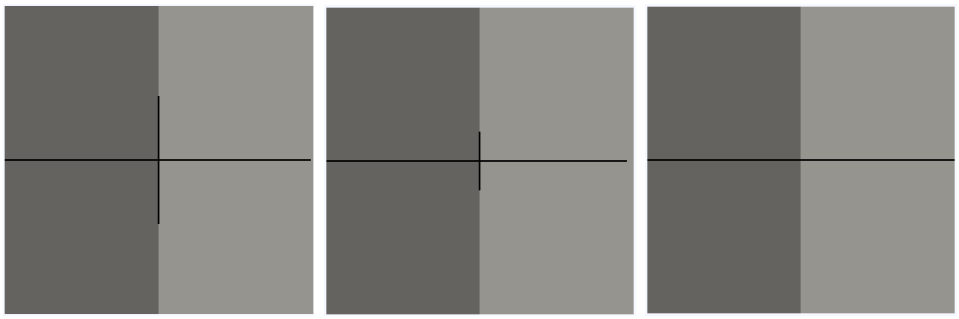

(a) $\sigma_{max}^{int} = 0.1(\sigma_{max}^{bulk})$. (b) $\sigma_{max}^{int} = 0.3(\sigma_{max}^{bulk})$. (c) $\sigma_{max}^{int} = 0.5(\sigma_{max}^{bulk})$.

Figure 9: Final crack paths for $E_1 = 210$ GPa, $E_2 = 420$ GPa.

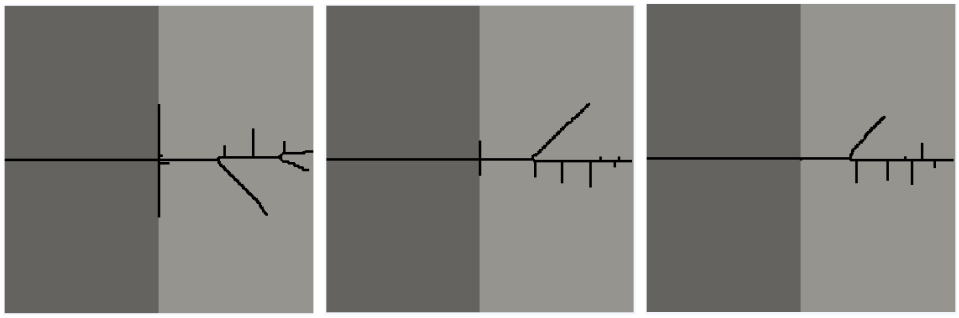

(a) $\sigma_{max}^{int} = 0.2(\sigma_{max}^{bulk})$. (b) $\sigma_{max}^{int} = 0.4(\sigma_{max}^{bulk})$. (c) $\sigma_{max}^{int} = 0.6(\sigma_{max}^{bulk})$.

Figure 10: Final crack paths for $E_1 = 210$ GPa, $E_2 = 630$ GPa.

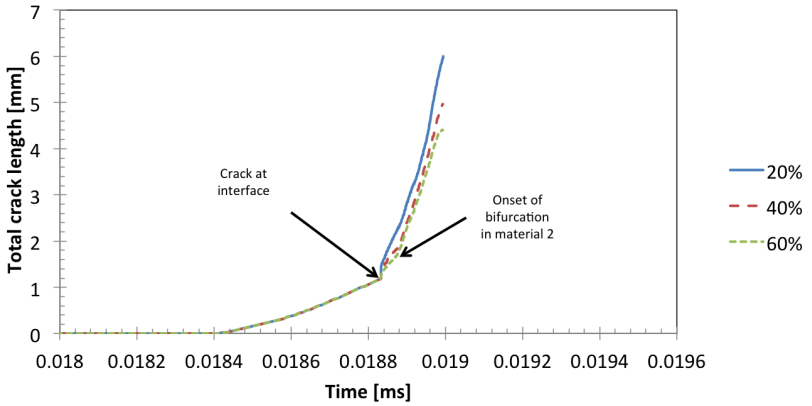

Figure 11: Crack length history for $E_1 = 210$ GPa, $E_2 = 630$ GPa and $\sigma_{max}^{int}/\sigma_{max}^{bulk} = 0.2$, 0.4 and 0.6.

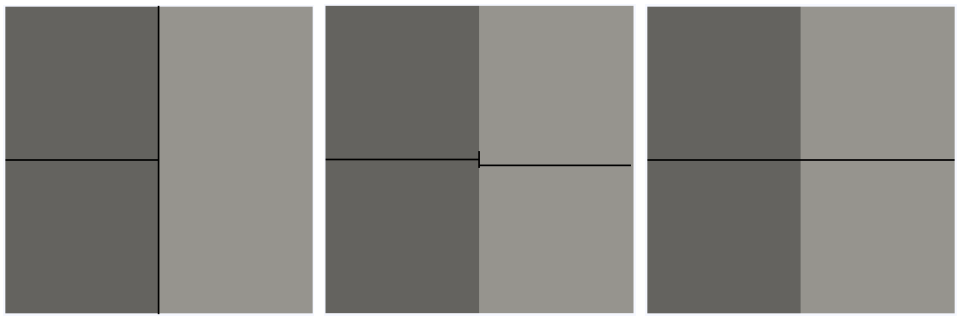

(a) $\sigma_{max}^{int} = 0.1(\sigma_{max}^{bulk})$. (b) $\sigma_{max}^{int} = 0.2(\sigma_{max}^{bulk})$. (c) $\sigma_{max}^{int} = 0.3(\sigma_{max}^{bulk})$.

Figure 12: Final crack paths for $E_1 = 210$ GPa, $E_2 = 105$ GPa.

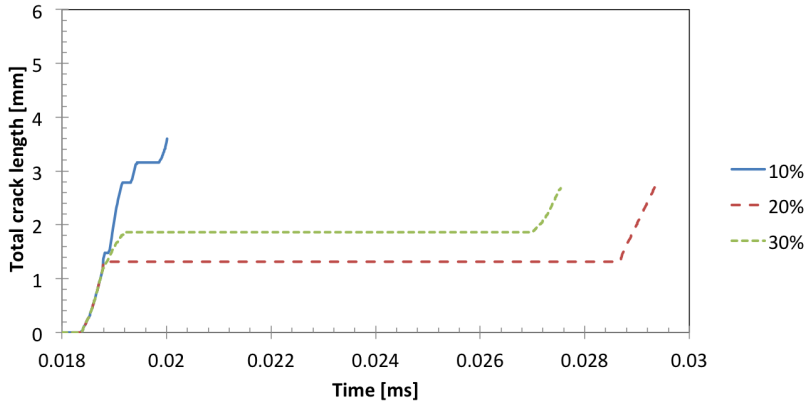

Figure 13: Crack length history for $E_1 = 210$ GPa, $E_2 = 105$ GPa and $\sigma_{max}^{int}/\sigma_{max}^{bulk} = 0.1$, 0.2 and 0.3.